J|A|C|S
ARTICLES
Published on Web 03/11/2003

Tuning the Photoinduced Electron-Transfer Thermodynamics in 1,3,5-Triaryl-2-pyrazoline Fluorophores: X-ray Structures, Photophysical Characterization, Computational Analysis, and in Vivo Evaluation

Christoph J. Fahrni,* Liuchun Yang, and Donald G. VanDerveer

Contribution from the School of Chemistry and Biochemistry, Georgia Institute of Technology, 770 State Street, Atlanta, Georgia 30332

Received August 23, 2002; E-mail: fahrni@chemistry.gatech.edu

Abstract: A series of donor-substituted 1,3,5-triaryl-2-pyrazoline fluorophores were structurally characterized by X-ray analysis, and their photophysical properties studied by steady-state absorption and emission spectroscopy. The photoinduced electron-transfer thermodynamics of the derivatives was estimated on the basis of the spectroscopic data and redox potentials of the fluorophores. The aryl substituents in the 1- and 3-position of the pyrazoline ring influence the photophysical properties of the fluorophores in distinctly different ways. The excited-state equilibrium energy ΔE_{00} is primarily influenced by changes of the substituent in the 1-position, whereas the reduction potential of the fluorophore is essentially determined by the 3-aryl group. Density functional calculations were used to probe the electronic structure and energy ordering of the emissive and the electron-transfer state. The results from the computational analysis agree qualitatively well with the experimental data. In addition, we have evaluated a water soluble pyrazoline derivative in vivo as a potential intracellular pH probe. Membrane permeability, low toxicity, and high quantum yield render the fluorophore attractive for biological applications.

Introduction

Fluorescent probes are powerful tools in cell biology for the noninvasive measurement of intracellular ion concentrations.[1] They have found widespread applications, for example, to gauge intracellular calcium concentrations,[2] to visualize labile zinc[3−8] and iron pools,[9] or as pH sensors.[10] Based on their molecular architecture, the probes can be divided into two major classes. The cation receptor moiety is either an integral part of the fluorophore, as in intrinsic fluorescent probes, or separated by a spacer.[11] The latter utilizes a fast photoinduced electron-transfer process (PET) to translate the binding event into a visible change of the fluorescence output. In the absence of the analyte, the fluorescence is quenched due to photoinduced electron transfer between the receptor and fluorophore, whereas upon binding of the cation the thermodynamics of the quenching process is rendered unfavorable and the fluorescence emission is "switched on". If the excited-state equilibrium energy, as well as the oxidation and reduction potential of the receptor and fluorophore, is known, the thermodynamics of the quenching process can be estimated on the basis of the Rehm−Weller formalism.[12] Therefore, to design a fluorescent probe, a cation specific receptor acting as the electron donor must be combined with a fluorophore that matches the appropriate reduction potential. If the fluorophore synthesis provides sufficient structural flexibility, the excited-state equilibrium energy and reduction potential can be adjusted accordingly, for example, by attaching electron-withdrawing or -donating substituents.

Fluorescein and rhodamine derivatives are presumably the most widely used fluorophores in biological research.[13] Their visible excitation wavelength, high quantum yield, cell permeability, and water solubility are favorable properties for the design of cation-specific fluorescent probes, or simply as fluorescent tags for proteins or small molecules such as lipids or sugars. Unfortunately, the synthesis of even simple derivatives involves often tedious multistep procedures accompanied by low overall yields[3,7,14] and is therefore a serious limitation for tuning of their photophysical properties. Clearly, for the design of

(1) Mason, W. T. *Fluorescent and Luminescent Probes for Biological Activity: A Practical Guide to Technology for Quantitative Real-time Analysis*; Academic Press: San Diego, CA, 1999.
(2) Takahashi, A.; Camacho, P.; Lechleiter, J. D.; Herman, B. *Physiol. Rev.* **1999**, *79*, 1089.
(3) Burdette, S. C.; Walkup, G. K.; Spingler, B.; Tsien, R. Y.; Lippard, S. J. *J. Am. Chem. Soc.* **2001**, *123*, 7831.
(4) Nasir, M. S.; Fahrni, C. J.; Suhy, D. A.; Kolodsick, K. J.; Singer, C. P.; O'Halloran, T. V. *J. Biol. Inorg. Chem.* **1999**, *4*, 775.
(5) Zalewski, P. D.; Millard, S. H.; Forbes, I. J.; Kapaniris, O.; Slavotinek, A.; Betts, W. H.; Ward, A. D.; Lincoln, S. F.; Mahadevan, I. *J. Histochem. Cytochem.* **1994**, *42*, 877.
(6) Frederickson, C. J.; Kasarskis, E. J.; Ringo, D.; Frederickson, R. E. *J. Neurosci. Methods* **1987**, *20*, 91.
(7) Hirano, T.; Kikuchi, K.; Urano, Y.; Nagano, T. *J. Am. Chem. Soc.* **2002**, *124*, 6555.
(8) Gee, K. R.; Zhou, Z. L.; Ton-That, D.; Sensi, S. L.; Weiss, J. H. *Cell Calcium* **2002**, *31*, 245.
(9) Esposito, B. P.; Epsztejn, S.; Breuer, W.; Cabantchik, Z. I. *Anal. Biochem.* **2002**, *304*, 1.
(10) Takahashi, A.; Zhang, Y. P.; Centonze, V. E.; Herman, B. *Biotechniques* **2001**, *30*, 804.
(11) Valeur, B.; Leray, I. *Coord. Chem. Rev.* **2000**, *205*, 3.
(12) Rehm, D.; Weller, A. *Isr. J. Chem.* **1970**, *8*, 259.
(13) Haugland, R. P. *Handbook of Fluorescent Probes and Research Chemicals*; Molecular Probes: Eugene, OR, 2002.
(14) Gee, K. R.; Zhou, Z. L.; Qian, W. J.; Kennedy, R. *J. Am. Chem. Soc.* **2002**, *124*, 776.

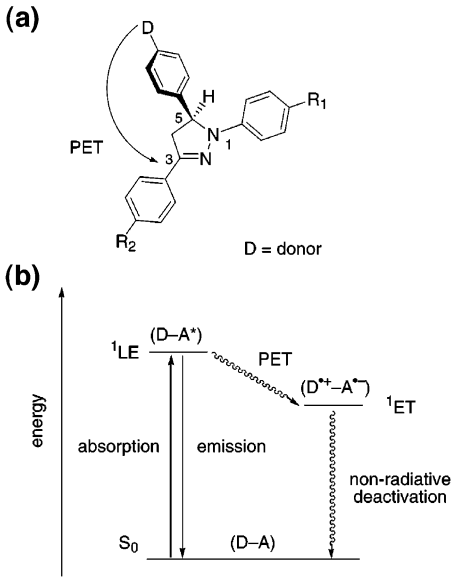

Figure 1. Photoinduced electron transfer (PET) in 1,3,5-triaryl-2-pyrazolines. (a) Fluorophore with electronically decoupled donor group (D); (b) simplified Jablonski diagram for the ET process of a pyrazoline-based donor−acceptor system (D−A) (S_0, singlet ground state; ^{1}LE, emissive locally excited singlet state; ^{1}ET, electron-transfer state). Vibrational relaxation and solvent stabilization effects are not included in the diagram.

cation specific fluorescent probes, a synthetically more flexible fluorophore structure would be desirable.

Among possible substitutes, pyrazoline-based fluorophores stand out due to their simple structure and favorable photophysical properties such as large extinction coefficient and quantum yields ($\Phi_f \approx 0.6-0.8$).[15,16] The synthesis of 1,3,5-triaryl-substituted pyrazoline fluorophores is readily accomplished by two condensation reactions and provides, due to its modular nature, a high degree of structural flexibility.[16,17] Despite their attractive properties, surprisingly few applications, including cation- or pH-sensitive probes, have been described,[18−24] and the suitability of pyrazoline fluorophores as probes in a biological environment is still unexplored.

The rigid molecular architecture is well suited for the design of PET-based fluorescent probes. A donor unit can be covalently linked with the aryl spacer in the 5-position of the pyrazoline ring, resulting in a donor−spacer−acceptor system (Figure 1a).[19,20,23−25] The actual chromophoric π-system is composed of the two aryl substituents in the 1- and 3-position and three out of the five pyrazoline ring atoms (N1−N2−C3). The remaining two carbon atoms (C4 and C5) of the ring are sp^3 hybridized and are not part of the conjugated π-system.

Chart 1

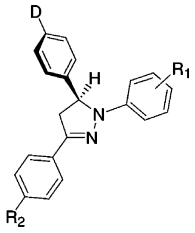

	R_1	R_2	D
1a	H	H	NEt_2
1b		CN	
1c		COOEt	
2a	4-CN	H	NEt_2
2b		CN	
2c		COOEt	
2d		OMe	
2e		COOH	
3a	2,3,4,5,6-F_5	H	NEt_2
3b		COOEt	
4a	4-OMe	CN	NEt_2
4b		COOEt	
5	4-F	COOEt	NEt_2
6	4-CN	COOEt	H

As shown by Rurack et al.,[24] the photophysical properties of donor-substituted pyrazolines are principally determined by the relative energy of the excited state localized on the fluorophore (^{1}LE) and a highly polarized state (^{1}ET), which is formed upon excitation via ultrafast intramolecular electron transfer between the donor (D) and the fluorophore moiety (Figure 1b). Whereas emission from the locally excited state ^{1}LE occurs typically with high quantum yield, the electron-transfer state ^{1}ET is nonemissive. The aryl substituents in the 1- and 3-position determine the excited-state energy and redox properties of the fluorophore, and thus influence the thermodynamics of the excited-state electron-transfer quenching process. Therefore, the photophysical properties of the fluorophore can be adjusted with a suitable choice of the pyrazoline substituents. If the locally excited state LE for a molecule with a specific combination of R_1 and R_2 is higher in energy compared to the electron-transfer state ET, the fluorescence is expected to be quenched. In the reversed case, the excited-state electron transfer is thermodynamically unfavorable, and emission from the locally excited state LE occurs. Due to the highly polarized nature of the ET state, the relative energy ordering of the two states (ET and LE) depends also on the solvent polarity. In a nonpolar solvent, the ET state is less stabilized compared to a polar solvent which lowers the excited-state energy via dipole−dipole interactions. The solvent dependence of the quenching thermodynamics is an intrinsic property of PET-based fluorophores and might be an interfering factor in biological applications. In a cellular context, the probe is exposed to a variety of different polarities, such as the cytoplasm or the low polarity environment of lipid bilayers. To avoid misinterpretations and artifacts, detailed studies of the subcellular distribution of cation-sensitive fluorophores are therefore of great importance.

In this work, we have systematically explored the photoinduced electron-transfer thermodynamics of 1,3,5-triaryl-substituted pyrazolines as a function of the aryl substituents in the 1- and 3-position. A series of 13 pyrazoline derivatives **1**−**5** have been synthesized, which all contain a diethylamino group as an electron-transfer donor and various electron-donating or -withdrawing substituents attached to the 1- and 3-aryl rings (Chart 1). The fluorophores have been characterized by steady-state absorption and fluorescence emission spectroscopy, and the electron-transfer thermodynamics has been estimated on the basis of the spectroscopic data and redox potentials. To probe the electronic structure and energy ordering of the LE and ET states, we have carried out density functional calculations (DFT)

(15) Güsten, H.; Heinrich, G. *Ber. Bunsen-Ges. Phys. Chem.* **1977**, *81*, 810.
(16) Rivett, D. E.; Rosevear, J.; Wilshire, J. F. K. *Aust. J. Chem.* **1983**, *36*, 1649.
(17) Wagner, A.; Schellhammer, C. W.; Petersen, S. *Angew. Chem., Int. Ed. Engl.* **1966**, *5*, 699.
(18) de Silva, A. P.; de Silva, S. A.; Dissanayake, A. S.; Sandanayake, K. *Chem. Commun.* **1989**, 1054.
(19) de Silva, A. P.; Gunaratne, H. Q. N. *Chem. Commun.* **1990**, 186.
(20) de Silva, A. P.; Gunaratne, H. Q. N.; Maguire, G. E. M. *Chem. Commun.* **1994**, 1213.
(21) de Silva, A. P.; Gunaratne, H. Q. N.; Lynch, P. L. M. *J. Chem. Soc., Perkin Trans. 2* **1995**, 685.
(22) de Silva, A. P.; Gunaratne, H. Q. N.; Gunnlaugsson, T.; Nieuwenhuizen, M. *Chem. Commun.* **1996**, 1967.
(23) Rurack, K.; Resch-Genger, U.; Bricks, J. L.; Spieles, M. *Chem. Commun.* **2000**, 2103.
(24) Rurack, K.; Bricks, J. L.; Schulz, B.; Maus, M.; Reck, G.; Resch-Genger, U. *J. Phys. Chem. A* **2000**, *104*, 6171.
(25) Yan, Z. L.; Wu, S. K. *J. Luminescence* **1993**, *54*, 303.

and correlated the theoretical data with the experimental results. In addition, we have characterized the properties of carboxylic acid derivative (**2e**) in aqueous solution and evaluated the fluorophore in vivo as a potential intracellular pH probe. The major impetus for this work was to gain detailed insights into the photophysics of this compound class and, hence, to provide a basis for the rational design of cation specific fluorescent probes in a biological environment.

Experimental Section

Synthesis. All compounds were prepared using synthetic protocols developed for 1,3,5-triaryl-2-pyrazoline derivatives.[16] The crude products were purified by flash chromatography, and the purity of the final products was tested by reversed-phase HPLC (Varian ProStar system with UV detector, acetonitrile−water, gradient 20% → 2% water). The chemical structures of the synthesized compounds were confirmed by ^{1}H NMR, MS, and high-resolution mass spectrometry (HRMS). Description of the syntheses and detailed analytical data are provided with the Supporting Information.

Steady-State Absorption and Fluorescence Spectroscopy. All sample solutions were filtered through 0.45 μm Teflon membrane filters to remove interfering dust particles or fibers. UV−vis absorption spectra were recorded at 25 °C using a Varian Cary Bio50 UV−vis spectrometer with a constant-temperature accessory. Steady-state emission and excitation spectra were recorded with a PTI fluorimeter and FELIX software. For all measurements, the path length was 1 cm with a cell volume of 3.0 mL. The fluorescence spectra have been corrected for the spectral response of the detection system (emission correction file provided by instrument manufacturer) and for the spectral irradiance of the excitation channel (via calibrated photodiode). Quantum yields were determined using quinine sulfate dihydrate in 1.0 N H_2SO_4 as a fluorescence standard ($\Phi_f = 0.54 \pm 0.05$).[26]

Electrode Calibration in Aqueous Solution. Measurements were performed with an Orion combination glass microelectrode (model 9802BN). For the determination of p*K* values in aqueous solution, the electrode was calibrated for $-\log[H_3O^+]$ by titration of a standardized HCl solution (Aldrich, 0.1 N volumetric standard) with KOH (Aldrich, 0.1 N volumetric standard) at 25 °C and 0.1 M ionic strength (KCl). The end point, $E°$, and slope were determined using Gran's method[27] as implemented in the software GLEE.[28] The electrode potential was measured with the Corning pH/Ion Analyzer 355, and the emf measurements were reproducible with ±0.1 mV accuracy.

Determination of p*K* Values. The fluorescence emission spectra of the fluorophore were monitored for a series of solutions in which $-\log[H_3O^+]$ was varied between 5 and 9. The emf of each solution was directly measured in the fluorescence quartz cell (electrode diameter 3 mm) and converted to $-\log[H_3O^+]$ using $E°$ and slope as obtained from the electrode calibration procedure described previously. The raw spectral and emf data were processed via nonlinear least-squares fit analysis using the SPECFIT software package.[29]

Cyclic Voltammetry. The cyclic voltammograms were acquired in acetonitrile (freshly distilled over calcium hydride) containing 0.1 M Bu_4NPF_6 as electrolyte using a CH-Instruments potentiostat (model 600A). The samples were measured under inert gas at a concentration of 3 mM in a single compartment cell with a Pt working and counter electrode and an Ag/AgCl reference electrode. The half-wave potentials were referenced to ferrocene as the internal standard, and the measurements were typically performed with 500 mV s^{-1} scan rate.

X-ray Structure Analysis. Crystals of **1b**, **2a**−**d**, and **3b** suitable for X-ray structural analysis were grown from acetonitrile−water by slow evaporation of the solvent over a period of several days. The X-ray data were collected on a Siemens SMART 1K CCD diffractometer with graphite-monochromated Mo Kα radiation (λ = 0.71073 Å). The programs SADABS (Sheldrick)[30] and SAINT 6.22 (Bruker)[31] were used for absorption corrections. The structure was solved by direct methods and refined by least-squares calculations with the SHELXTL 5.10 software package.[31] The hydrogen atoms were added using ideal geometries with a fixed C−H bond distance of 0.96 Å. A summary of the crystallographic parameters and data is included with the Supporting Information (Tables S1 and S3).

Computational Methods. All calculations were carried out with the Q-Chem electronic structure calculation suite of programs.[32] The geometries of ground-state structures were optimized by the density functional method using Becke's gradient corrected three-parameter exchange functional[33] with the correlation functional of Lee, Yang, and Parr[34] (B3LYP). The split-valence polarized 6-31G* (6-31G(d)) basis set was used for all geometry optimizations. Single point energies were computed at the B3LYP/6-31G* level using the optimized geometry (B3LYP/6-31G*//B3LYP/6-31G*). To obtain estimates of the vertical electronic excitation energies which include some account of electron correlation, time-dependent density functional theory (TD-DFT)[35] calculations with the B3LYP functional and 6-31G* basis set were performed. The calculation of ground-state potential curves is based on relaxed geometries with the corresponding constraints of dihedral angles. Molecular orbitals were visualized with the software MOLEKEL[36] using the Q-Chem plot output data. Details for all computations including the coordinates of the geometry-optimized structures are provided with the Supporting Information (Tables S4 and S5).

Cell Culture Experiments. HeLa cells were cultivated in Dulbecco's modified Eagle medium (DMEM) supplemented with 5% calf serum and 200 mM L-glutamine. For the uptake experiments, cells were coincubated with 50 nM Lysotracker Red (Molecular Probes) and 5 μM pyrazoline **2c** for 60 min at 37 °C, washed 3 times with PBS, and fixed with 3.7% paraformaldehyde for 30 min before mounting on slides with Fluoromount[13] (Molecular Probes). To equilibrate intracellular pH gradients, cells were incubated with 1 μM nigericine (Sigma) for 30 min prior to incubation with the dyes. The cells were analyzed using an Olympus microscope (BX40, plan apo 60×, 1.40) equipped with a standard fluorescence excitation filter set. For quantization of the fluorescence intensity over a large cell population (10 000 counts), cells were analyzed with a Becton−Dickinson LSR flow cytometer.

Preparation of Liposomes. The liposomal experiment was performed at a lipid concentration of 1 mg/mL PIPES buffer solution (10 mM PIPES, 0.1 KNO_3). The solution was prepared by evaporation of 1.0 mL of lipid solution (20 mg/mL 1,2-dioleoyl-*sn*-glycero-3-phosphocholine in chloroform). After addition of 2.0 mL of PIPES buffer solution, the mixture was allowed to hydrate for 1 h. The mixture was then ultrasonicated until the solution clarified and the final concentration was adjusted to 1 mg/mL.

Results and Discussion

1. Structural Studies. Pyrazoline derivatives **1**−**6** were synthesized from *p*-diethylamino-benzaldehyde or benzaldehyde

(26) Demas, J. N.; Crosby, G. A. *J. Phys. Chem.* **1971**, *75*, 991.
(27) Gran, G. *Analyst (London)* **1951**, *77*, 661.
(28) Gans, P.; O'Sullivan, B. *Talanta* **2000**, *51*, 33.
(29) Binstead, R. A.; Zuberbühler, A. D. *SPECFIT Global Analysis System*, 3.0.27 ed.; Spectrum Software Associates: Marlborough, MA, 01752, 2001.
(30) Blessing, R. H. *Acta Crystallogr., Sect. A* **1995**, *51*, 33.
(31) *SHELXTL 5.10*; Bruker: Madison, WI, 1998.
(32) Kong, J.; White, C. A.; Krylov, A. I.; Sherrill, C. D.; Adamson, R. D.; Furlani, T. R.; Lee, M. S.; Lee, A. M.; Gwaltney, S. R.; Adams, T. R.; Ochsenfeld, C.; Gilbert, A. T. B.; Kedziora, G. S.; Rassolov, V. A.; Maurice, D. R.; Nair, N.; Shao, Y.; Besley, N. A.; Maslen, P. E.; Dombroski, J. P.; Dachsel, H.; Zhang, W. M.; Korambath, P. P.; Baker, J.; Byrd, E. F. C.; Voorhis, T. V.; Oumi, M.; Hirata, S.; Hsu, C. P.; Ishikawa, N.; Florian, J.; Warshel, A.; Johnson, B. G.; Gill, P. M. W.; Head-Gordon, M.; Pople, J. A. *Q-Chem*, 2.0 ed.; Q-Chem Inc.: Export, PA, 2000.
(33) Becke, A. D. *J. Chem. Phys.* **1993**, *98*, 5648.
(34) Lee, C. T.; Yang, W. T.; Parr, R. G. *Phys. Rev. B* **1988**, *37*, 785.
(35) Stratmann, R. E.; Scuseria, G. E.; Frisch, M. J. *J. Chem. Phys.* **1998**, *109*, 8218.
(36) Flükiger, P.; Lüthi, H. P.; Portmann, S.; Weber, J. *MOLEKEL 4.1*, 4.1 ed.; Swiss Center for Scientific Computing: Manno, Switzerland, 2000−2001.

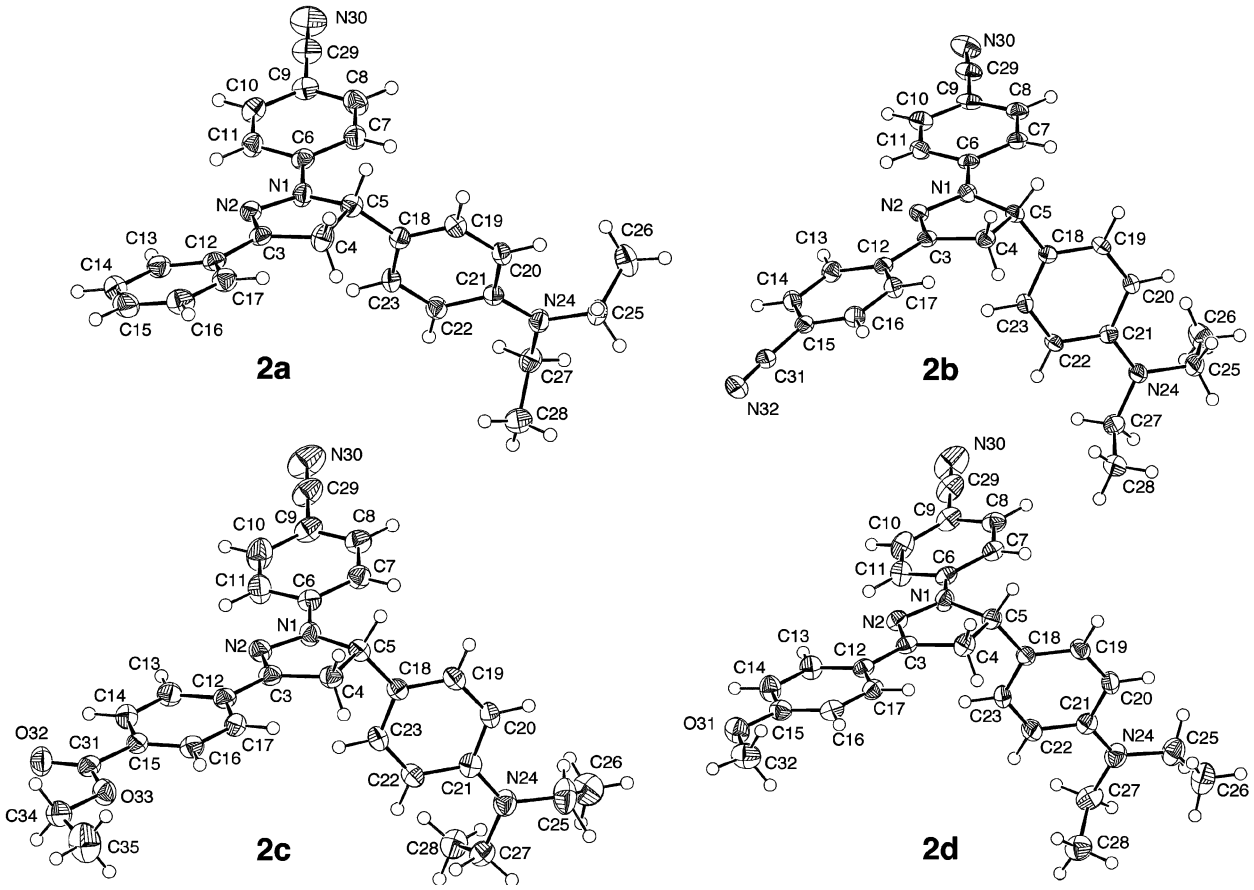

Figure 2. X-ray structures and numbering schemes showing the (*S*) isomer of pyrazoline derivatives **2a**−**d**. Thermal ellipsoids are drawn at the 50% level.

Table 1. Selected Structural Data for Pyrazoline Derivatives **1b**, **2a**, **2b**, **2c**, **2d**, and **3b**

parameter	**1b**[a]	**2a**	**2b**	**2c**	**2d**	**3b** (A)	**3b** (B)[e]
N(1)−N(2) (Å)	1.376(4)	1.379(2)	1.373(2)	1.374(2)	1.379(2)	1.377(8)	1.380(8)
N(1)−C(5) (Å)	1.493(4)	1.482(2)	1.496(2)	1.483(2)	1.490(2)	1.515(9)	1.496(9)
N(1)−C(6) (Å)	1.384(5)	1.380(2)	1.379(2)	1.377(2)	1.373(2)	1.382(10)	1.373(9)
N(2)−C(3) (Å)	1.291(5)	1.291(2)	1.296(2)	1.292(2)	1.297(2)	1.300(10)	1.287(9)
C(3)−C(12) (Å)	1.449(5)	1.463(2)	1.458(3)	1.462(3)	1.459(2)	1.431(9)	1.456(9)
C(3)−C(4) (Å)	1.512(5)	1.499(2)	1.515(2)	1.504(3)	1.501(2)	1.509(10)	1.502(10)
N(2)−C(3)−C(12) (deg)	120.9(3)	121.58(13)	122.13(16)	120.52(16)	121.20(15)	121.5(6)	120.6(6)
C(6)−N(1)−N(2) (deg)	119.9(3)	119.74(11)	119.42(14)	119.56(15)	120.34(13)	119.8(6)	119.2(5)
N(1)−C(5)−C(18) (deg)	112.7(3)	113.40(14)	112.44(13)	112.21(15)	110.96(13)	111.2(5)	112.5(5)
N(l)−C(5)−C(18)−C(23) (θ_1)[b] (deg)	−48.6(4)	−34.63(13)	−63.6(2)	−54.2(2)	−46.9(2)	−58.5(9)	−47.0(8)[f]
N(2)−N(1)−C(6)−C(11) (θ_2)[b] (deg)	−3.6(6)	8.1(2)	0.6(2)	−7.8(3)	−4.2(2)	−2.4(8)	−32.8(10)[f]
N(2)−C(3)−C(12)−C(13) (θ_3)[b] (deg)	10.9(6)	−8.5(2)	8.8(2)	0.5(3)	4.0(2)	4.7(8)	−0.5(10)[f]
$\sum_1$ at N(l)[c] (deg)	359.9	357.86	359.73	359.65	358.56	357.9	358.8
$\sum_2$ at C(3)[d] (deg)	360.0	359.94	359.98	360.0	359.98	359.9	359.9

[a] ORTEP plot and numbering scheme in Supporting Information. [b] Dihedral angles refer to the (*S*) stereoisomer. [c] Sum of bond angles N2−N1−C6, N2−N1−C5, and C5−N1−C6. [d] Sum of bond angles N2−C3−C12, C4−C3−C12, and N2−C3−C4. [e] Crystallographically independent conformations with opposite chirality. [f] (*S*) isomer.

by aldol condensation with the corresponding acetylphenyl derivative followed by cyclization with various substituted phenylhydrazines as described in the literature for similar compounds.[16] Slow evaporation from acetonitrile−water provided X-ray quality crystals for derivatives **1b**, **2a**−**d**, and **3b**. The ORTEP plots and atomic numbering schemes of the structures are shown in Figures 2 and 3, and selected structural parameters are compiled in Table 1. Despite the relatively rigid molecular framework of 1,3,5-triaryl pyrazolines, the observed structural differences are significant. The phenyl ring in the 5-position of the pyrazoline ring shows the largest conformational flexibility among the three aryl substituents, which is reflected in considerable variations of dihedral angle θ_1 ranging from −34° to −63°. Consistent with this observation, quantum chemical calculations of the potential energy curve for rotation around the C5−C18 bond axis reveal a relatively shallow minimum (vide infra). The nitrogen atom of the diethylamino group is planar in all structures, suggesting significant interactions of the lone pair electrons with the aromatic π-system. The delocalization of electron density from the nitrogen atom to the neighboring aromatic ring is further supported by the partial double-bond character of the N24−C21 bond (average 1.376 ± 0.002 Å), which is in all structures considerably shorter compared to the N24−C25 single bond (average 1.460 ± 0.015 Å). Given the rotational flexibility of the ethyl group, it is not surprising that several different conformations were found for

Chart 2

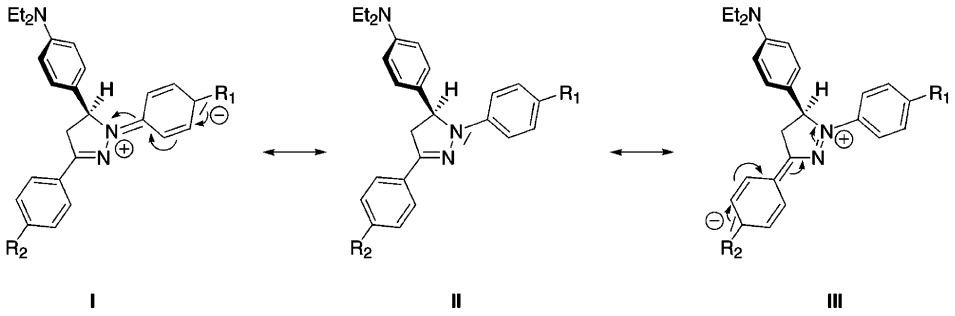

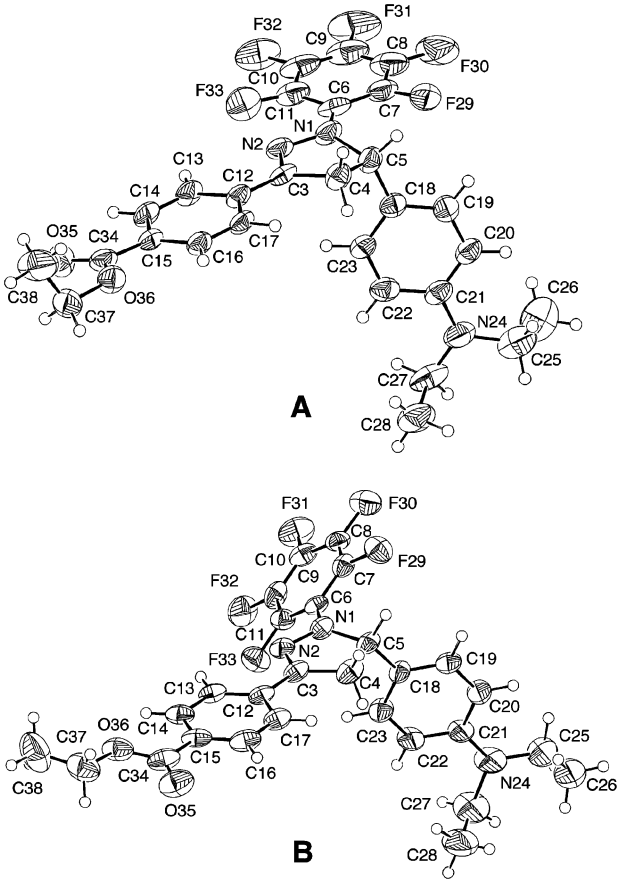

Figure 3. X-ray structure and numbering schemes for pyrazoline derivative **3b**. The two conformations (A and B) are crystallographically unique. For better comparison, both (*S*) isomers are depicted. Thermal ellipsoids are drawn at the 50% level.

the diethylamino substituent. The crystal structure of **2c** shows even a disordered orientation of the ethyl group (only one orientation is shown in Figure 2).

The other two phenyl groups in the 1- and 3-position exhibit much smaller conformational variations. Both dihedral angles θ_2 and θ_3 deviate only a few degrees from an ideal coplanar orientation between the phenyl ring and the pyrazoline π-system (Table 1). Consistent with a pronounced electronic interaction, the bond distances of these two aryl groups to the pyrazoline ring are significantly shorter as would be expected for a single bond. The unit cell of the crystal structure of the pentafluorophenyl-substituted derivative **3b** contains two crystallographically independent molecules with substantially different conformations. Notably, the pentafluorophenyl ring in one of the conformations (B) is twisted along the N1−C6 bond axis ($\theta_2 = -32.8°$), whereas conformation A shows a coplanar orientation with the pyrazoline ring and a dihedral angle of $-2.4°$.

The variations of bond lengths within the pyrazoline π-system reflect differences in the degree of charge delocalization, as illustrated by the Lewis structures in Chart 2. The two aryl substituents are electronically separated and communicate only indirectly via the "Janus-faced" lone pair localized on the pyrazoline nitrogen N1. This electron lone pair can be delocalized toward either the aryl ring in the 1-position (Chart 2, structure I) or the aryl substituent in the 3-position (structure III). The degree of delocalization will vary as a function of the electron-donating or -withdrawing character of the substituents R_1 and R_2.

According to the data listed in Table 1, the differences are most prominent for the C3−C12 bond, which varies significantly as a function of R_2. For example, the increased electron-withdrawing character of the cyano group in **2b** shortens the bond from 1.463 to 1.458 Å compared to the unsubstituted derivative **2a**. In pyrazoline **1b**, which allows even greater charge delocalization due to the electron-richer nitrogen N1, the bond is further shortened to 1.449 Å. Analogously, with increasing electron-withdrawing character of substituent R_1, the bond distance N1−C6 is decreasing. The additional cyano substituent in derivative **2b** shortens the bond to 1.379 Å compared to 1.384 Å in **1b**. With the electron-donating methoxy substituent R_2 in **2d**, the bond length is even further decreased to 1.373 Å.

2. Photophysical Studies. 2.1. Steady-State Absorption and Emission. In view of potential applications as sensor molecules in a biological environment, the spectroscopic measurements should preferably be carried out in aqueous solution. Due to the limited water solubility of the synthesized pyrazoline derivatives, methanol was chosen as a substitute. In addition, the water-soluble free acid **2e** was synthesized and spectroscopically characterized under physiological conditions at pH 7.20.

2.1.1. UV−vis Spectra. The absorption spectra plotted in Figure 4 (left) are arranged according to the aryl substituent R_2 in the 3-position of the pyrazoline ring. All spectra are characterized by a strong, featureless absorption band centered around 24 000−26 000 cm^{-1}, which is only shifted to substantially higher energy in the case of the pentafluorophenyl derivatives **3a** and **3b** (Figure 4a and c). The energy maxima of this band are compiled in Table 2 together with other spectroscopic information of the synthesized derivatives. Based on the results of DFT calculations discussed in section 2.3, the band can be assigned to an allowed $\pi \rightarrow \pi^*$ transition localized on the pyrazoline ring system and therefore corresponds to

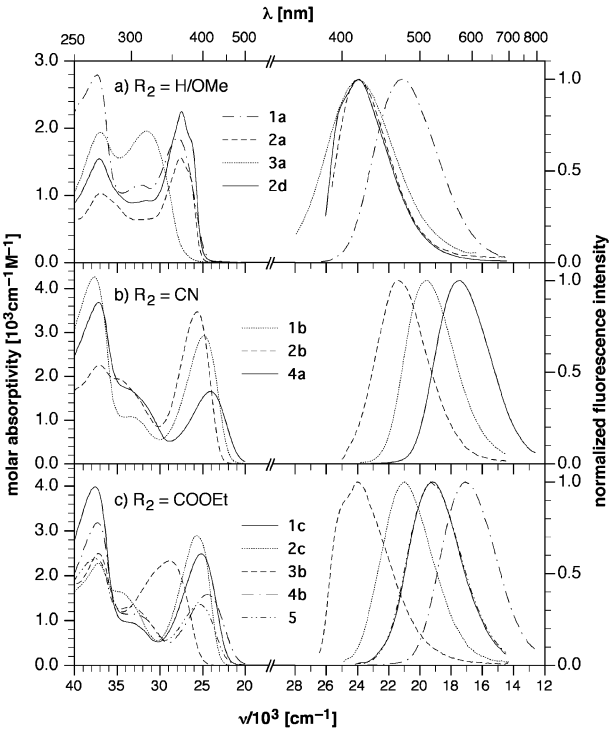

Figure 4. UV absorption (left) and normalized emission spectra (right) of pyrazolines **1**−**5** in methanol at room temperature.

Table 2. Room Temperature Photophysical Data of Pyrazolines **1**−**6** in Methanol at Neutral and Acidic pH

compd	ν_{abs} [cm^{-1}] neutral	ν_{abs} [cm^{-1}] acidic[a]	ν_{em}[b] [cm^{-1}]	$\nu_{abs}-\nu_{em}$[c] [cm^{-1}]	Φ_f[d] neutral	Φ_f[d] acidic	ef[e]
1a	27 990	28 240	21 128	6 750	0.11	0.24	2
1b	25 350	25 350	19 650	5 700	0.04	0.29	7
1c	25 190	25 773	19 080	6110	0.02	0.52	37
2a	27 620	28 010	24 000	3620	0.01	0.57	50
2b	25 640	26 590	21 390	4250	0.011	0.43	40
2c	25 700	26 320	20 960	4740	0.011	0.59	55
2d	27 470	27 770	23 920	3550	0.032	0.20	6
3a	31 560	32 680	28 330	3230	0.004	0.004	1
3b	28 820	29 760	22 080	6740	0.004	0.66	160
4a	24 090	24 630	17 480	6610	0.12	0.12	1
4b	24 450	25 000	17 090	7360	0.11	0.11	1
5	25 380	25 910	19 260	6120	0.028	0.40	14
6	26 050	26 050	20 880	5170	0.63	0.62	1

[a] 0.1% trifluoroacetic acid in methanol. [b] Determined for acidic conditions only. [c] Stokes' shift under acidic conditions. [d] Quantum yield determined with quinine sulfate in 1.0 N H_2SO_4 as reference. [e] Fluorescence enhancement factor between neutral and acidic solutions (based on quantum yield).

excitation to the ^{1}LE state, as shown in Figure 1b. The quantum chemical calculations also suggest a considerable charge-transfer character for this transition, which is influenced by the nature of the pyrazoline substituents. For a given substituent R_2, the absorption energy is slightly increasing with increasing electron-withdrawing character of the *N*-phenyl substituent R_1. For example, the *p*-methoxyphenyl derivative **4a** shows an absorption maximum at 24 090 cm^{-1}, whereas the phenyl (**1b**) and *p*-cyanophenyl (**2b**) derivatives are shifted to 25 350 and 25 640 cm^{-1}, respectively (Figure 4b). Furthermore, the absorption band shifts to lower energy with increasing electron-withdrawing character of the substituents R_2. Interestingly, an electron-donating group such as the methoxy-phenyl substituent in **2d** does not further shift the absorption maximum to higher energy.

2.1.2. Emission Spectra. Whereas the absorption energy appears to be rather insensitive toward changes in the substitution patterns, the emission maxima are significantly influenced and vary by more than 7000 cm^{-1} (Figure 4). As observed for the absorption spectra, the emission maxima shift to higher energy with increasing electron-withdrawing character of the substituent R_1. Charge-transfer states are effectively stabilized in polar media such as methanol and water, due to dipole−dipole interaction of the polarized excited-state with the solvent. Therefore, with increasing charge-transfer character of the excited state, the Stokes' shift is expected to increase. With decreasing electron-withdrawing character of the substituent in the 1-position, the lone pair electrons on N1 are more delocalized toward the 3-substituted phenyl ring, and hence the charge-transfer character of the emissive state is increasing. This effect can be observed consistently for all derivatives. For example, the *p*-cyano-substituted pyrazolines **1b**, **2b**, and **4a** (Figure 4b) exhibit a gradually increasing Stokes' shift going from 4250 to 5700, and 6610 cm^{-1} with decreasing electron-withdrawing character of the substituents on the 3-phenyl ring. Similarly, the Stokes' shift is increasing from 3230 to 3620, and 6750 cm^{-1} for the N1-phenyl substituted series **3a**, **2a**, and **1a** (Figure 4a). The donor strength of the N1 electron lone pair is maximized with an electron-donating substituent such as the *p*-methoxyphenyl group. Combination with an electron-acceptor as in the *p*-cyanophenyl-substituted derivative **4a** results in a large Stokes' shift of 6610 cm^{-1}. The reverse combination with the *p*-methoxyphenyl group attached in the 3-position and an electron-withdrawing cyano substituent at the N1-position, as in **2d**, decreases the Stokes' shift dramatically to 3550 cm^{-1}. In summary, the 1,3,5-triaryl-substituted pyrazoline fluorophores exhibit great flexibility for tuning the absorption and emission properties, and the measured data are in agreement with the spectroscopic trends of similar, previously characterized 1,3- and 1,3,5-aryl-substituted pyrazolines.[15,16]

2.1.3. Quantum Yields. The aryl substituents in the 1- and 3-position not only influence the absorption and emission energy of the molecule but also determine the redox properties of the fluorophore, and thus influence the thermodynamics of the excited-state electron-transfer quenching process. The quantum yield of the fluorescence emission gives valuable insights into the efficiency of the quenching process. Moreover, protonation of the diethylamino group, which is acting as the electron-donor moiety in the excited-state electron-transfer process, is expected to increase the donor oxidation potential and should therefore inhibit the quenching pathway. Indeed, the fluorescence quantum yield for most of the pyrazoline derivatives **1**−**5** increases significantly in the presence of 0.1% trifluoroacetic acid (Figure 5) and approaches an average value around 0.5. It is noteworthy that emission of both of the *p*-methoxy-substituted derivatives **4a** and **4b** remains unchanged upon protonation but already exhibits a significant quantum yield of 0.1 in neat methanol. The quantum yields in neutral and acidic methanol for all derivatives are listed in Table 2. A more detailed discussion of the observed emission intensity changes follows the quantitative analysis of the electron-transfer thermodynamics (section 2.3).

2.1.4. Solvatochromic Shift and Excited-State Dipole Moments. An analysis of the Stokes' shift as a function of solvent polarity gives an estimate of the difference between excited-state and ground-state dipole moments, which is indica-

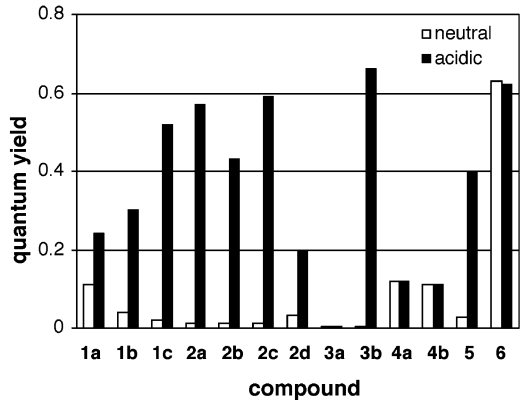

Figure 5. Comparison of the emission quantum yields in neutral and acidic methanol containing 0.1% trifluoroacetic acid.

tive for the extent of the charge-transfer process occurring in the excited state. The absorption and emission spectra of all derivatives were acquired in four solvents covering a large polarity range (cyclohexane, diethyl ether, ethyl acetate, and acetonitrile), and the data were analyzed employing the Lippert−Mataga formalism (eqs 1 and 2).[37−39] A compilation of all absorption and emission data is added to the Supporting Information (Table S2). According to the Lippert−Mataga formalism, a plot of the Stokes' shift $\Delta\bar{\nu}_{(abs-em)}$ versus the solvent polarity function $\Delta f = f(\epsilon_s) - f(n)$ allows for determination of the difference between the excited-state and ground-state dipole moments ($\mu_e - \mu_g$) via linear regression:

$$\Delta\bar{\nu} = \bar{\nu}_{abs} - \bar{\nu}_{em} = \Delta\bar{\nu}_0 + \frac{2}{hc}\frac{(\mu_e - \mu_g)^2}{a_0^3}\Delta f \qquad (1)$$

with

$$\Delta f = f(\epsilon_s) - f(n) = \frac{\epsilon_s - 1}{2\epsilon_s + 1} - \frac{n^2 - 1}{2n^2 + 1} \qquad (2)$$

where a_0 is the Onsager cavity radius,[40] ϵ_s and n are the relative permittivity and refractive index of the corresponding solvent, respectively, and $\Delta\bar{\nu}_0$ is the extrapolated Stokes' shift in a vacuum. If the ground-state dipole moment of the molecule is known, the excited-state dipole moment can be estimated from the slope.

With the exception of **2d**, all pyrazoline derivatives exhibit a considerably larger dipole moment in the excited state compared to the ground state (Table 3). As previously concluded from the absorption and emission data acquired in methanol, the charge-transfer character increases with the increasing electron-withdrawing ability of the substituent R_2. For example, within the series of the *p*-cyanophenyl-substituted derivatives **2d**, **2a**, **2b**, and **2c**, the slope of the solvatochromic plots is gradually increasing from 452 to 4981, 5866, and 8024 cm^{-1} (Figure 6a).

The estimated excited-state dipole moments increase accordingly from 13.8 to 18.5, 19.3, and 22.6 D, respectively. Evidently, the strong electron-withdrawing ester group in **2c** results in an excited state with the greatest charge-transfer character and the largest dipole moment 22.6 D. In a polar solvent such as methanol or water, the excited state of this derivative is more effectively stabilized compared to the other compounds within the series, and therefore also yields the lowest emission energy (Table 2). A comparison of the solvatochromic shifts between derivatives with varying substituents R_1 but identical substituents R_2 reveals a different picture. Changes in the electron-withdrawing character of R_1 have no significant effect on the slope, as indicated by the parallel lines of the linear regression analysis (Figure 6b and c). Only the intercept $\Delta\bar{\nu}_0$,

Table 3. Slopes of the Solvatochromic Plots and Estimated Dipole Moments According to the Lippert−Mataga Model

compd	$2(\mu_e-\mu_g)^2/a_0^3$ [a] [cm^{-1}]	a_0 [b] [Å]	μ_g [D] (DFT) [c]	$\mu_e-\mu_g$ [D]	μ_e [d] [D]	d [e] [Å]
1a	5099	5.51	4.4	9.2	13.6	2.8
1b	8581	5.67	8.5	12.5	20.9	4.4
1c	8864	5.73	6.4	12.9	19.3	4.0
2a	4981	5.56	9.3	9.2	18.5	4.5
2b	5866	5.66	9.0	10.3	19.3	3.8
2c	8024	5.72	10.4	12.2	22.6	4.7
2d	452	5.69	10.9	2.9	13.8	2.9
3a	2744	5.39	5.0	6.5	11.5	2.4
3b	8673	5.81	7.0	12.9	20.0	4.2
4a	8309	5.52	8.2	11.8	19.9	4.1
4b	8803	5.69	5.3	12.7	17.9	3.7
5	7327	5.83	7.0	12.0	19.0	3.9
6	8136	5.49	9.2	11.6	20.7	4.3

[a] Slope of solvatochromic plot (from eq 1). [b] Onsager cavity radii a_0 were calculated from the molecular volumes based on X-ray data or geometry-optimized structures and increased by 0.5 Å to account for the first solvation shell (see Supporting Information for details). [c] Computed ground-state dipole moment (B3LYP/6-31G*//B3LYP/6-31G*). [d] Calculated based on computed μ_g. [e] Charge separation (1 D = 4.8 Å).

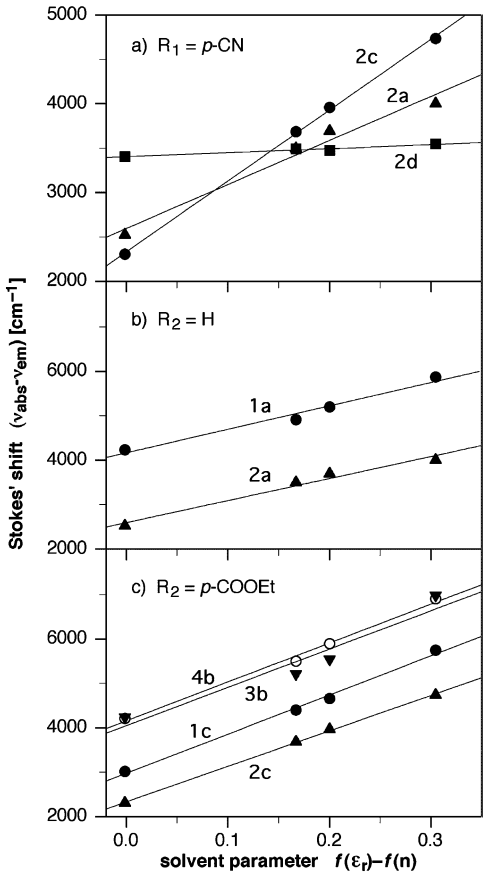

Figure 6. Solvatochromic shifts as a function of the solvent polarity parameter Δf according to the Lippert−Mataga formalism (eq 1).

(37) Lippert, E. *Z. Elektrochem.* **1957**, *61*, 962.
(38) Lippert, E. *Z. Naturforsch.* **1955**, *10A*, 541.
(39) Mataga, N.; Kaifu, Y.; Koizumi, M. *Bull. Chem. Soc. Jpn.* **1956**, *29*, 465.
(40) Onsager, L. *J. Am. Chem. Soc.* **1936**, *58*, 1486.

Table 4. Redox Potentials for Pyrazolines **1**−**6** in Acetonitrile/0.1 M Bu_4NPF_6 vs Fc/Fc^+

compd	$E_{1/2}$(ox) [V]			$E_{1/2}$(red) [V]	
1a	0.37	0.51		−2.82[a]	
1b	0.41	0.60		−2.27[b]	−2.57
1c	0.40	0.56		−2.30	−2.68
2a	0.42	0.77		−2.63	
2b	0.44	0.87		−2.14	−2.56
2c	0.43	0.84		−2.19	−2.56
2d	0.43	0.54[b]	1.03	−2.80	
3a	0.42[b]	0.92[b]		−2.70	
3b	0.43[b]	0.99[b]		−2.24	−2.78[a]
4a	0.29	0.54[a]	0.98	−2.28	−2.53
4b	0.24	0.53	1.02[a]	−2.30	−2.84
5	0.41	0.61[b]		−2.29	−2.49
6		0.78		−2.17	−2.41

[a] Not resolved. [b] Reversible.

which corresponds to the extrapolated Stokes' shift in a vacuum, is considerably changed. Conclusively, the two substituents R_1 and R_2 influence the charge-transfer process in the excited state in two distinctly different ways. The change of dipole moments between ground and excited state is primarily determined by R_2, which is therefore the major determinant for the magnitude of the solvatochromic shifts.

2.2. Redox Properties and Electron-Transfer Thermodynamics. The free energy change for the electron-transfer reaction $(D-A^*) \rightarrow (D^{\bullet+}-A^{\bullet-})$ between an excited-state acceptor (A*) and ground-state donor (D) can be estimated using the Rehm−Weller expression,[12,41]

$$\Delta G_{ET} = E_{1/2}(D^+/D) - E_{1/2}(A/A^-) - \Delta G_{00} - w_p \quad (3)$$

where $E_{1/2}(D^+/D)$ and $E_{1/2}(A/A^-)$ are the ground-state redox potentials of the donor and acceptor moiety, respectively, and ΔG_{00} is the free energy change for the transition between the ground state and the vibrationally relaxed excited state of the precursor (D−A*). Further details about the estimation of the solvent dependent work term w_p and solvent specific corrections are given with the Supporting Information.

2.2.1. Cyclic Voltammetry. To analyze quantitatively the electron-transfer thermodynamics according to the Rehm−Weller equation (eq 3), the redox potentials of all pyrazoline derivatives **1**−**6** were measured (Table 4).

Almost all compounds are oxidized irreversibly within a rather narrow potential range of 0.37−0.43 V. This first oxidation step is evidently independent from the substituents R_1 and R_2 and can be attributed to removal of an electron from the 5-aryl diethylamino group. Compound **6**, which is lacking the diethylamino substituent, shows a greater oxidation potential of 0.78 V, which is consistent with the assignment. Only the two pyrazolines **4a** and **4b** with the electron-rich 1-anisyl substituent exhibit a distinctively lower potential of 0.29 and 0.24 V, respectively. Interestingly, the oxidation potential of the 3-anisyl-substituted derivative **2d** is not lowered but still shows a third oxidation around 1 V as also observed for **4a** and **4b**. Apparently, the electron-donating methoxy group sufficiently lowers the oxidation potential only in the case of the electron-rich 1-*N*-aryl but not the 3-aryl substituent. Consequently, removal of the first electron occurs preferably from this site and not from the diethylamino group.

(41) Kavarnos, G. J. *Fundamentals of Photoinduced Electron Transfer*; VCH Publishers: New York, 1993.

Table 5. Electron Transfer Parameters and Quantum Yields of Pyrazolines **1**−**5** in Methanol

compd	ΔE_{00}[a] [eV]	$E_{1/2}$[b] (D^+/D) [eV]	$E_{1/2}$[b] (A/A^-) [eV]	ΔG_{ET}[c] [eV]	Φ_f[d]	ef[e]
1a	3.05	0.37	−2.82	0.10	0.11	2
1b	2.76	0.41	−2.27	−0.12	0.04	7
1c	2.74	0.40	−2.30	−0.09	0.02	37
2a	3.20	0.42	−2.63	−0.19	0.01	50
2b	2.92	0.44	−2.14	−0.38	0.01	40
2c	2.89	0.43	−2.19	−0.31	0.01	55
2d	3.19	0.43	−2.80	−0.00	0.03	6
3a	3.71	0.42	−2.70	−0.63	0.004	1
3b	3.16	0.43	−2.24	−0.53	0.004	160
4a	2.58	0.29	−2.28	−0.05	0.12	1
4b	2.58	0.24	−2.30	−0.08	0.11	1
5	2.77	0.41	−2.29	−0.11	0.03	14

[a] Estimated from normalized absorption and emission spectra. [b] Halfway potential measured in acetonitrile/0.1 M Bu_4NPF_6 vs Fc/Fc^+. [c] Calculated based on eq 3 as described in the Supporting Information. [d] Quantum yield in methanol. [e] Fluorescence enhancement factor upon protonation (0.1% trifluoroacetic acid in methanol).

In contrast, the first reduction step is distributed over a larger potential range (−2.1 to −2.8 V) and clearly varies as a function of the aryl groups R_1 and R_2. No significant difference can be observed between the reduction potential of compound **6**, which is missing the diethylamino substituent, and its analogue **2c**. Consequently, the first reduction step involves addition of an electron to the 1,3-diaryl-pyrazoline moiety to form the radical anion of the fluorophore. Derivatives containing at least one electron-withdrawing substituent, such as CN or COOEt, exhibit consistently a second reduction step between −2.4 and −2.8 V. It is noteworthy that for a given substituent R_2 the first reduction step occurs in a rather narrow potential range. For example, all of the ethyl carboxylate derivatives **1c**, **2c**, **3b**, **4b**, and **5** are reduced around −2.25 V, regardless of the nature of R_1. An analogous comparison of a series of compounds with identical substituent R_1 reveals a strong dependence on R_2. Thus, the *p*-cyanophenyl-substituted derivatives **2a**, **2b**, **2c**, and **2d** cover a large potential range from −2.14 to −2.80 V with variation of R_2.

2.2.2. Photoinduced Electron-Transfer Thermodynamics. The free energy change ΔG_{ET} associated with the excited-state electron-transfer reaction $(D-A^*) \rightarrow (D^{\bullet+}-A^{\bullet-})$ in the pyrazoline derivatives **1**−**5** were calculated employing the Rehm−Weller equation (eq 3). The resulting data compiled in Table 5 reveal that the two aryl substituents R_1 and R_2 influence the electron-transfer process in distinctly different ways. For convenient comparison, the quantum yields and fluorescence enhancement factors between neutral and acidic methanol are also included in Table 5.

For a given substituent R_2, the thermodynamic driving force increases with increasing electron-withdrawing character of R_1. For example, in the series of the ethyl carboxylate pyrazolines **1c**, **5**, **2c**, and **3b**, the free energy change ΔG_{ET} becomes gradually more favorable and decreases from −0.09 to −0.11, −0.31, and finally −0.53 eV. The emission quantum yields in neutral methanol are decreasing in the same order, which is consistent with the increased efficiency of the photoinduced ET quenching process. As pointed out in the previous section, the first reduction potential of 1,3-diaryl pyrazolines is primarily determined by the nature of the aryl substituent in the 3-position, whereas the 1-*N*-aryl group displays only little influence. Therefore, changes in the thermodynamic driving force of the

ET process in the series **1c**, **5**, **2c**, and **3b** must be due to differences in the equilibrium energy ΔE_{00}, which changes as a function of R_1. Indeed, with increasing electron-withdrawing character of R_1, the emission energy is gradually increasing (Table 2) and therefore enhancing also the equilibrium energy ΔE_{00} (Table 5).

A comparison of the ET driving force for a series with identical substituent R_1 but varying R_2 reveals a different trend. The quantum yields of the pyrazoline derivatives **2a**, **2b**, and **2c** are virtually identical, and the fluorescence enhancement factors (ef) upon protonation show only small variations. Nevertheless, derivative **2d** with the electron-rich methoxy substituent significantly reduces the reduction potential of the fluorophore, which renders the thermodynamics of the ET quenching process less favorable. Consequently, the emission quantum yield of the unprotonated fluorophore increases, and the observed enhancement factor is significantly lower. A similar effect can be observed for the pyrazolines **1a** and **1c** (or **1b**). The unsubstituted 3-aryl ring gives rise to a substantially lower reduction potential in **1a** compared to **1c**, which contains an electron-withdrawing ester group. The ET quenching process of **1a** in neutral methanol is consequently less favorable compared to that of **1c**, which is in line with the greater emission quantum yield of 0.11 in neutral methanol.

The quantum yield of the two 1-*N*-anisyl-substituted derivatives **4a** and **4b** does not undergo any changes upon protonation with trifluoroacetic acid. Due to the substantial charge-transfer character, the ^{1}LE state is effectively stabilized in methanol and the resulting equilibrium energy ΔE_{00} is significantly lower compared to those of all other derivatives (Table 5). Furthermore, the first oxidation potential of these two electron-rich derivatives is substantially lower than expected for removal of an electron from the diethylamino donor group (Table 4). Evidently, the emission quenching process is not due to ET from the diethylamino group and must involve a different mechanism.

The analysis of the ET process according to the Rehm−Weller formalism provides valuable information about the thermodynamic efficiency of the quenching process but not necessarily about its inhibition upon protonation with trifluoroacetic acid. To understand the protonation induced changes in the emission quantum yields, it is necessary to consider the energy difference and relative ordering of the emissive ^{1}LE and nonemissive ^{1}ET levels. Protonation of the diethylamino group increases the oxidation potential of the donor and raises therefore the ^{1}ET level. Nevertheless, a large fluorescence enhancement factor is only observed, if the ^{1}ET level rises sufficiently above the energy of the emissive ^{1}LE level (Figure 1).

2.3. Quantum Chemical Calculations. Since the ^{1}ET state undergoes only nonradiative deactivation, it is not possible to spectroscopically measure its energy. Instead, quantum chemical calculations can be used to better rationalize the observed fluorescence changes upon protonation. Rurack et al. recently reported molecular orbital calculations to probe the ET thermodynamics of donor-substituted 1,3,5-triaryl pyrazolines but only at the semiempirical level using AM1-optimized geometries (ZINDO//AM1).[24] To provide reliable state energies and electronic structures for the pyrazoline derivatives **1**−**6**, we optimized the geometries and calculated the ground- and excited-state electronic structures at the B3LYP/6-31G*//B3LYP/6-31G* level.

Table 6. Selected Computed[a] Structural Data for 1,3,5-Triaryl Pyrazolines **1**−**5**

compd	C(6)–N(1) (Å)	N(1)–N(2) (Å)	N(2)–C(3) (Å)	C(3)–C(12) (Å)	Σ_1[b] (deg)	Σ_2[c] (deg)
1a	1.399	1.366	1.294	1.463	357.10	359.99
1b	1.399	1.353	1.298	1.456	359.59	360.0
1c	1.397	1.356	1.298	1.458	359.79	360.0
2a	1.383	1.368	1.294	1.463	359.55	359.99
2b	1.387	1.359	1.296	1.459	359.95	359.99
2c	1.385	1.363	1.295	1.460	359.82	360.0
2d	1.381	1.372	1.294	1.460	354.22	359.99
3a	1.394	1.375	1.293	1.464	354.93	359.97
3b	1.386	1.363	1.295	1.460	359.82	360.0
4a	1.404	1.352	1.299	1.456	358.41	360.0
4b	1.404	1.356	1.298	1.456	357.90	360.0
5	1.399	1.358	1.297	1.458	358.55	360.0

[a] Geometry-optimized structures from DFT calculations (B3LYP/6-31G*). [b] Sum of bond angles at N1 (N2−N1−C5, N2−N1−C6, C5−N1−C6). [c] Sum of bond angles at C3 (N2−C3−C12, C4−C3−C12, N2−C3−C4).

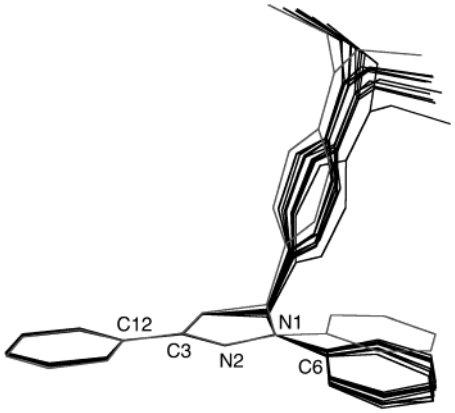

Figure 7. Overlay of the calculated geometry-optimized structures for pyrazolines **1**−**5** at the B3LYP/6-31G* level (grey, predicted geometry for **3b**).

2.3.1. Geometry-Optimized Structures. To minimize artifacts due to conformational differences between the various derivatives, the X-ray-structure coordinates of **2b** were used as a "template" for all calculations. The substituents R_1 and R_2 were attached using standard bond lengths and angles, and the resulting structures were geometrically optimized. The computed key structural parameters are compiled in Table 6 and agree generally well with the crystal structure geometries (Table 1). Only the dihedral angle θ_1 (N1−C5−C18−C19), which reflects the relative orientation between the 5-aryl and the pyrazoline ring, deviates significantly from the crystal structure geometries. The potential energy curve calculated for rotation around the C4−C6 bond axis in derivative **2b** reveals a shallow energy minimum and a rather low activation barrier of 28.3 kJ mol^{-1} (data not shown). Given the small energy difference of 3.6 kJ mol^{-1}, computed for two conformers for which θ_1 differs as much as 20°, the deviation of the dihedral angles can well be attributed to packing forces in the solid state.

An overlay of the geometry-optimized structures of **1**−**5** reveals significant variability for the substituents in the 1- and 5-position, whereas the geometry around the 3-substituted aryl group is virtually identical for all derivatives (Figure 7). The various degrees of pyramidalization at the N1-nitrogen atom influence the geometry of the pyrazoline ring and therefore also the orientation of the substituents on the neighboring carbon C5. The sum of bond angles at carbon C3 (Σ_2) is 360° for all computed structures, which is indicative of a coplanar orientation

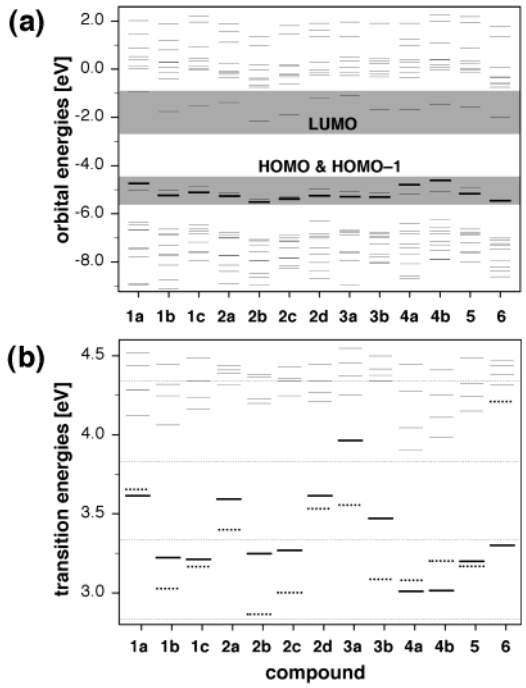

Figure 8. Results of TD-DFT calculations for pyrazolines **1**−**6**: (a) orbital energy diagram covering all MOs between HOMO−10 and LUMO+10, (b) transition energies for the six lowest-lying singlet states (LE state: bold lines, ET state: dotted lines).

of the aryl and pyrazoline ring (Table 6). In contrast, the sum of bond angles at N1 (Σ_1) is smaller than 360° for most derivatives, reflecting a partly tetrahedral conformation, which is in line with the experimentally determined geometries (Table 1).

As discussed previously for the crystal structure geometries, the substituents R_1 and R_2 influence the bond lengths of the pyrazoline core. In particular, the two bonds between N1 and its neighboring atoms C6 and N2 show significant changes across the various derivatives **1**−**5**, reflecting differences in the ground-state electronic structures. For example, with increasing electron-withdrawing character of the substituent R_2, the bond lengths N1−N2 gradually decrease in the series **2d**, **2a**, and **2b**, whereas N1−C6 follows the opposite trend (Table 6). Both changes are consistent with an increased charge delocalization toward R_2, as reflected by Lewis structure III (Chart 2). In contrast, with increasing electron-withdrawing character of substituent R_1, the bond lengths N1−C6 are decreasing in the series **4a**, **1b**, and **2b**, but the distance N1−N2 is slightly increasing. In this case, the charge delocalization can be described with Lewis structure I showing an increased bond order for N1−C6.

2.3.2. Ground- and Excited-State Electronic Structures. The computational analysis of the ground-state electronic structures reveals that the energy range of the frontier orbitals is clearly separated from all other MOs with exception of the HOMO-1 (Figure 8a).

The HOMO energy levels are very similar for most derivatives and parallel the rather narrow range of the measured oxidation potentials (Table 4). Furthermore, the changes of the LUMO energies are consistent with the observed variations in the first reduction potentials. To further elucidate the nature of the lowest excited states ^{1}ET and ^{1}LE, we used time-dependent density functional theory (TD-DFT) to calculate the gas-phase

Table 7. Calculated Transition Energies for the Lowest Two Excited States in Pyrazolines **1**−**6**

compd	abs exp[a] [eV]	^{1}LE$^{gas\ b}$ [eV]	f^c	^{1}ET$^{gas\ b}$ [eV]	f^c	(^{1}ET − ^{3}ET) [eV]
la	3.47	3.61	0.757	3.65	0.009	0.00
1b	3.08	3.22	0.974	3.03	0.017	0.02
1c	3.12	3.21	0.883	3.17	0.106	0.07
2a	3.41	3.59	1.030	3.40	0.028	0.03
2b	3.18	3.25	1.124	2.86	0.022	0.02
2c	3.18	3.26	1.119	3.00	0.019	0.02
2d	3.41	3.61	1.168	3.53	0.106	0.04
3a	3.91	3.96	0.867	3.56	0.081	0.07
3b	3.57	3.47	1.027	3.09	0.049	0.01
4a	2.98	3.01	0.820	3.08	0.070	0.02
4b	3.03	3.01	0.850	3.20	0.020	0.02
5	3.15	3.20	0.918	3.17	0.012	0.02
6	3.23	3.30	1.102	4.21	0.011	0.11

[a] Taken from solution spectrum in methanol at 25 °C. [b] DFT calculation (B3LYP/6-31G*//B3LYP/6-31G*), state assignment based on orbital surface plots. [c] Oscillator strength.

Franck−Condon vertical excitation energies at the B3LYP/6-31G* level. Recent work by Stratmann et al. has shown that TD-DFT yields significantly better results compared to those of Hartree−Fock based methods such as the random-phase approximation (RPA) or single excitation configuration interaction (CIS).[35]

According to the TD-DFT calculations, the two lowest-energy singlet states are energetically well separated from the closest higher lying states across all derivatives (Figure 8b). Only one of the two states (bold lines in Figure 8b) exhibits a large oscillator strength around 1.0 (Table 7), suggesting an allowed transition. The lowest-energy absorption band of the UV spectra agrees well within 0.1−0.2 eV with the calculated energies (Table 7) and can be assigned to the transition $S_0 \rightarrow {}^1$LE. Both states involve excitation into the LUMO, which is qualitatively identical for all derivatives, as illustrated with the MO plots of various selected examples in Figure 9.

The occupied MO associated with the allowed transition is also qualitatively identical for all derivatives, but dependent on the nature of the substituents R_1 and R_2, the energy ordering varies and the orbital is identified either as HOMO or HOMO-1 (Figure 9).

The MO contributions for the two lowest-energy states are best visualized with the corresponding detachment−attachment density plots, as shown in Figure 10. The detachment densities (blue) of the allowed transition are concentrated on the 1-phenyl ring but can be found also on N1, N2, and C3 of the pyrazoline, whereas the attachment densities (red) are localized on the 3-phenyl ring and expand over to C3 and N1 of the ring system. Conclusively, there is significant orbital overlap, which accounts for the large oscillator strengths of this transition. Furthermore, the state is characterized by a considerable charge transfer, which is consistent with the solvatochromic shifts and increased excited-state dipole moments (Table 3). A comparison with the orbital plots in Figure 9 allows one to recognize readily the involved MOs of the transitions and shows that the plotted states are essentially constituted by pure MOs without mixing.

The attachment density of the second-lowest energy state is localized on the 3-phenyl ring and identical with the corresponding density of the ^{1}LE state. In contrast, the detachment density is mostly concentrated on the diethylamino-substituted phenyl ring, suggesting an electron transfer between the nitrogen donor moiety and the pyrazoline fluorophore (Figure 10).

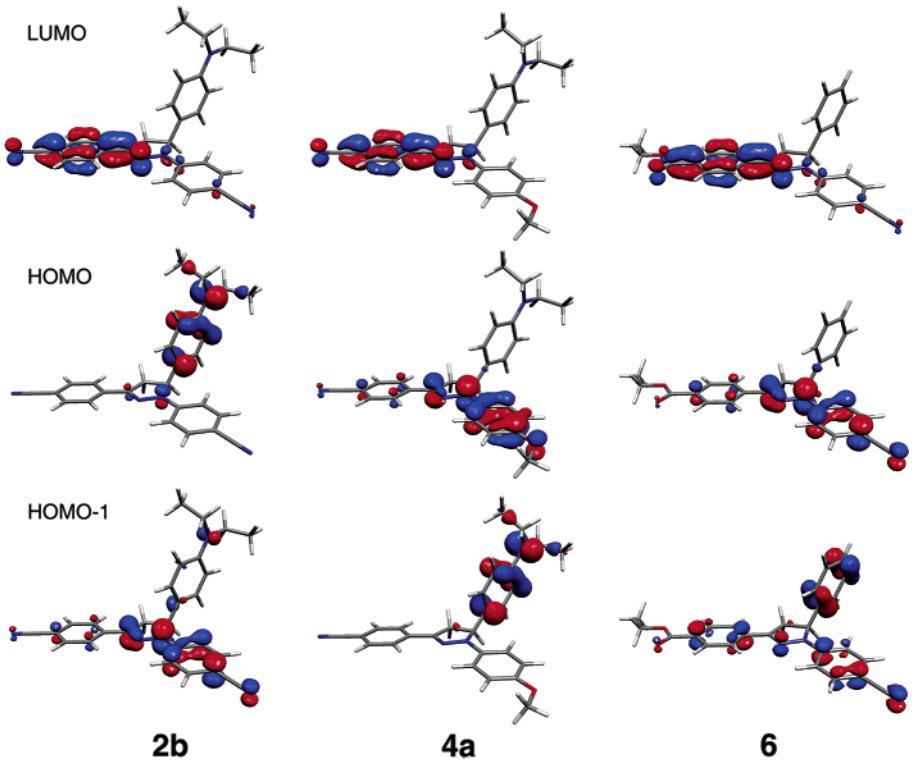

Figure 9. Molecular orbital plots for the HOMO−1, HOMO, and LUMO of pyrazoline derivatives **2b**, **4a**, and **6**.

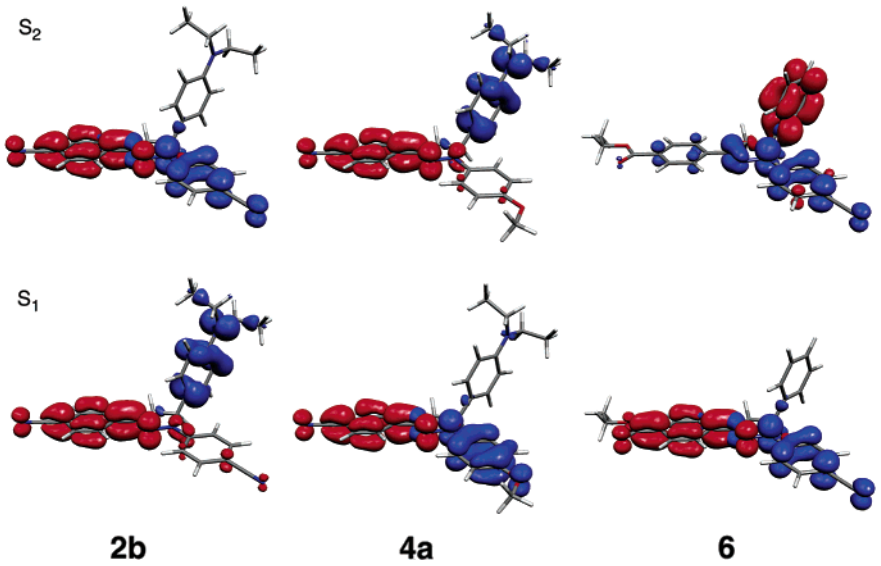

Figure 10. Detachment (blue) and attachment (red) density plots for the first (S_1) and second (S_2) excited states of pyrazoline derivatives **2b**, **4a**, and **6**.

The small energy gap to the neighboring triplet state further underlines the highly delocalized nature of this state (Table 7), which can unambiguously be assigned to the nonemissive ^{1}ET level. The energy ordering of the two states varies as a function of the substituents R_1 and R_2. For example, in **2d** the first excited singlet state S_1 corresponds to the electron-transfer state ^{1}ET, whereas S_2 can be assigned to the locally excited state ^{1}LE according to the detachment−attachment density analysis (Figure 10). In derivative **4a**, the S_1 state is qualitatively identical with S_2 of **2b**, and S_2 corresponds to S_1. The predicted energy ordering of the two states agrees well with the experimental data, which show efficient electron-transfer quenching for **2d** (^{1}ET is lower than ^{1}LE), but not for **4a** (^{1}ET is higher than ^{1}LE). In contrast, the energy difference between S_1 and S_2 in derivative **6**, which is lacking the diethylamino donor group, is substantially larger. The lowest lying state is qualitatively identical with the emissive state in **2b** and **4a**, whereas the high-energy singlet state S_2 does not resemble the ET state. In fact, the detachment−attachment density analysis for this state reveals a "reversed" electronic transition from the pyrazoline π-system to the 5-aryl substituent (Figure 10).

As expected, the ^{1}ET state (dashed lines) lies below the ^{1}LE state (bold lines) for most of the studied pyrazoline derivatives (Figure 8b). A reversed energy ordering is only observed for **1a**, **4a**, and **4b**, all of which exhibit unfavorable ET thermodynamics, as previously shown (Table 5), and an increased

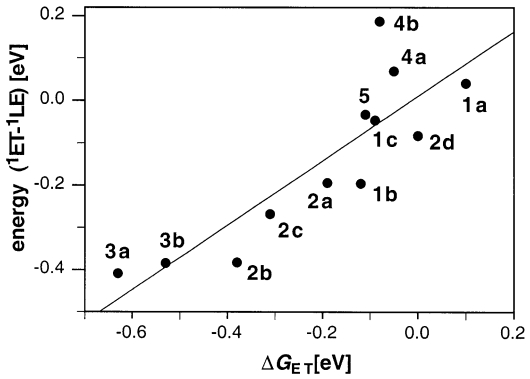

Figure 11. Correlation of the experimentally estimated free energy change of the photoinduced ET process (ΔG_{ET}) vs the calculated energy difference of the ^{1}LE and ^{1}ET states (B3LYP/6-31G*//B3LYP/6-31G*).

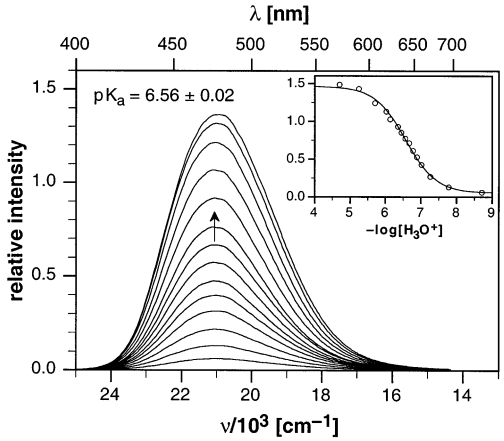

Figure 12. Fluorescence emission of pyrazoline **2e** as a function of pH (0.1 M KCl, 25 °C). Inset: fluorescence intensity at 475 nm and curve fit for determination of the protonation equilibrium constant (pK_a).

fluorescence emission quantum yield in neutral methanol (Table 2).

In the gas phase, the energy gap between the ^{1}LE and ^{1}ET states reflects principally the energy change associated with the ET process. A plot of the calculated excited-state energy differences versus the experimental free energy changes taken from Table 5 reveals a surprisingly good qualitative correlation (Figure 11). In agreement with the experimental data, the quantum chemical calculations reproduce qualitatively well the relative energy levels of the emissive LE and the nonemissive ET states. Nevertheless, it is important to remember that the calculated state energies refer to the vertical Franck−Condon excitation energies in the gas phase at 0 K, whereas the experimental data (for LE) are based on the vibrationally relaxed states in a polar solvent at room temperature. Due to the charge-separated nature of ET, the dipole moment of this state is typically larger compared to that of LE, and therefore, the energy stabilization in a polar medium is expected to be more significant. For example, the ET quenching for both derivatives **3a** and **3b** is very efficient with an estimated ΔG_{ET} of −0.63 and −0.50 eV, respectively (Table 5), but only derivative **3b** displays a dramatic fluorescence increase by a factor of 160 upon protonation. The calculated energy gap between LE and ET in the gas phase is almost identical for both derivatives (Figure 11), and therefore cannot account for the observed differences. The excited-state dipole moment of the emissive state in **3b**, however, is almost twice as large compared to that of **3a**. As a consequence, the LE state is better stabilized for **3b** in a polar solvent, which reduces the energy gap between LE and ET. Apparently, only in the case of **3b** the LE−ET energy gap is sufficiently low, such that the ET state rises above the LE state upon protonation and the emission is "switched on". The consideration of solvent effects as well as vibrational relaxation in the calculation of excited-state energies would provide more reliable data but is currently not implemented for TD-DFT in any of the commercially available electronic structure software packages.

3. Characterization under Physiological Conditions and Cell Biological Studies. The tunability of the photophysical properties combined with their synthetic flexibility render pyrazoline-based fluorophores very attractive targets for the development of fluorescent probes. In contrast to fluorescein- and rhodamine-based fluorophores, biologically relevant properties such as membrane permeability, toxicity, or subcellular distribution have not been investigated yet. The pH-responsive emission quantum yield of the studied pyrazoline derivatives has prompted us to evaluate them as possible selective markers for acidic organelles. Weakly basic amines generally accumulate in cellular compartments with low internal pH.[42,43] Protonation of the amino group yields a membrane impermeable cation, which remains trapped inside the organelle. Since pyrazoline **2c** exhibits superior solubility properties under physiological conditions, all cell biological studies were carried out with this derivative.

3.1. Potentiometry. To further improve the water solubility at neutral pH, the free acid **2e** was synthesized via hydrolysis of ester **2c**. The fluorometric pH titration shown in Figure 12 reveals a pK value of 6.56 ± 0.02 for protonation of the diethylamino group in **2e**. When the emission maximum of **2c** is compared, the emission maximum of **2e** is slightly shifted to higher energy (20 876 cm^{-1}), as would be expected based on the reduced electron-withdrawing character of the negatively charged carboxylate anion. The quantum yield increases from 0.02 to 0.30 upon protonation of the diethyl amino group in acidic medium (pH < 4.5). Based on these data, the basicity of the diethylamino group lies in the appropriate range for a lysosomotropic dye, and the membrane permeable derivative **2c** might be suitable to track intracellular pH gradients.

3.2. In-Vivo Evaluation. Incubation of HeLa cells with pyrazoline **2c** revealed a perinuclear punctate staining pattern (Figure 13a, middle). The carboxylate ester readily diffuses through the cell membrane and exhibits a surprisingly low toxicity. In a separate experiment, the cells were incubated for 3 h at a concentration of 5 μM, showing no visible signs of toxic effects. To further elucidate the nature of the stained compartments, HeLa cells were coincubated with Lysotracker Red, a commercially available fluorophore which specifically stains acidic organelles (Figure 13a, right).[13] Surprisingly, the false-color micrograph reveals no colocalization between Lysotracker and pyrazoline **2c**, which was additionally confirmed by confocal microscopy (data not shown).

To further investigate whether the observed staining pattern with **2c** is due to an ion trapping mechanism by organelles that

(42) Griffiths, G.; Hoflack, B.; Simons, K.; Mellman, I.; Kornfeld, S. *Cell* **1988**, *52*, 329.
(43) Anderson, R. G. W.; Falck, J. R.; Goldstein, J. L.; Brown, M. S. *Proc. Natl. Acad. Sci. U.S.A.* **1984**, *81*, 4838.

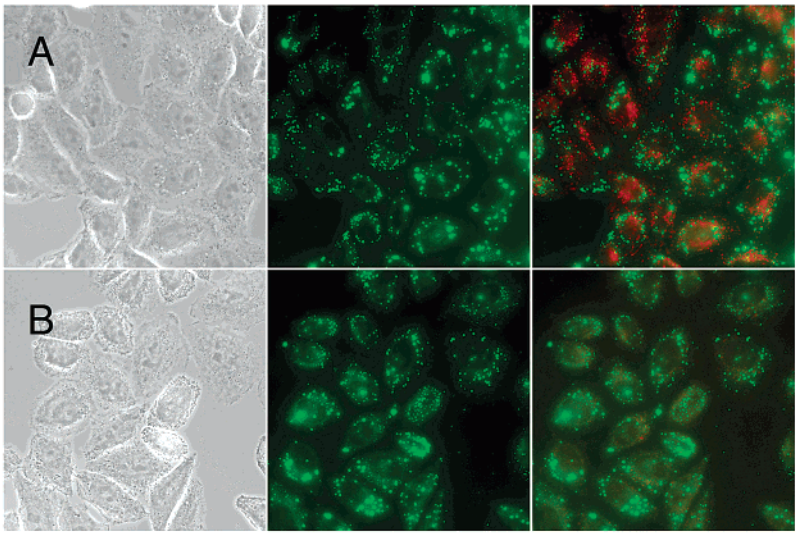

Figure 13. Phase images (left) and fluorescence micrographs for incubation of HeLa cells with pyrazoline **2c** (middle) and overlays with Lysotracker (right, false color image). (a) No pretreatment; (b) preincubation with 1 μM nigericine for 30 min at 37 °C.

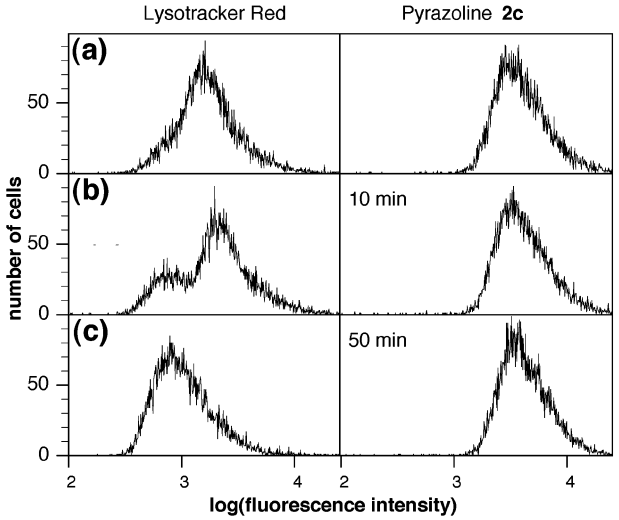

Figure 14. Flow cytometric analysis of HeLa cells incubated with Lysotracker (left) or pyrazoline **2c** (right) showing the effect of nigericine. The plots represent histograms of the fluorescence intensity distribution (population of 10 000 cells). (a) Control without nigericine. (b) 10 and (c) 50 min after addition of 1 μM nigericine to the cell suspension.

were not stained by the Lysotracker probe, we equilibrated intracellular pH gradients with nigericine. Incubation for 30 min with media containing 0.5−1 μM concentrations of the drug is generally sufficient to destroy intracellular pH gradients.[44] Indeed, the Lysotracker specific fluorescence disappears completely in an analogous incubation experiment with pH-equilibrated cells (Figure 13b). In contrast, the staining observed with **2c** remains unchanged even under these conditions, and therefore suggests a pH-independent mechanism for accumulation in the vacuolar structures. To assess quantitatively the fluorescence changes averaged over a large cell population, we performed a flow cytometric analysis (Figure 14). Cells were incubated for 90 min with a mixture of Lysotracker Red and pyrazoline **2c**, and after measurement of the initial fluorescence intensity for a population of 10 000 cells (Figure 14a), nigericine was added at a concentration of 1 μM. As shown in Figure 14b and c, the fluorescence signal of the Lysotracker probe undergoes a dramatic change, whereas the average fluorescence emission of **2c** remains unchanged. It is noteworthy that the flow cytometric analysis identifies two distinct cell populations upon treatment with nigericine. After an individual cell has taken up the drug, intracellular pH gradients are apparently quickly neutralized and the emission of the Lysotracker probe drops instantaneously.

(44) Millot, C.; Millot, J. M.; Morjani, H.; Desplaces, A.; Manfait, M. *J. Histochem. Cytochem.* **1997**, *45*, 1255.

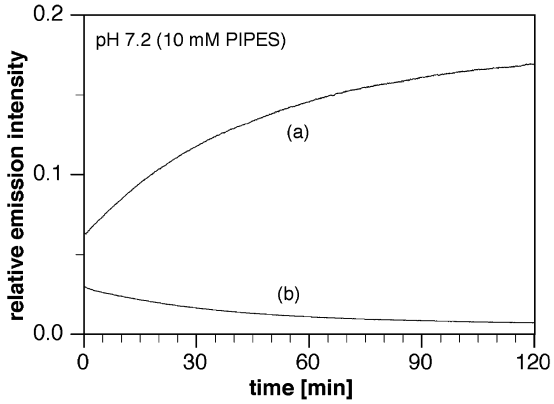

Figure 15. Fluorescence emission intensity of pyrazoline **2e** (20 μM) in the presence (a) and absence (b) of liposomes (1 mg/mL, PIPES 10 mM, 0.1 M KCl pH 7.20, 25 °C).

3.3. Model Studies with Liposomes. The incubation experiments with nigericine strongly suggest that the intracellular staining observed with **2c** is not due to an ion trapping mechanism of the protonated dye inside a low pH organelle. Since the thermodynamics of the electron-transfer quenching process is strongly dependent on the solvent polarity, the fluorescence enhancement might be due to partitioning of the dye into intracellular membrane structures. Because of the lower polarity of the membrane environment, the ET state might be sufficiently destabilized and rise above the emissive LE state. To test this hypothesis, we measured the fluorescence intensity of **2c** in the presence and absence of synthetic phospholipid vesicles (liposomes). Indeed, addition of pyrazoline **2c** to an aqueous solution of liposomes at pH 7.20 caused a 3-fold enhancement of the fluorescence intensity over a period of 2 h (Figure 15).

A control experiment without liposomes led to a slightly decreased fluorescence emission, presumably due to photodecomposition (bleaching) of the fluorophore. The observed shift of the peak emission to higher energy further supports the proposed mechanism, since not only the ET but also the emissive LE level has a larger dipole moment compared to the ground state (Table 3).

Conclusions

The structural flexibility of 1,3,5-triaryl pyrazoline allows for facile tuning of the photophysical properties. The substituents R_1 and R_2 influence the photoinduced electron-transfer thermodynamics of the investigated donor-substituted fluorophores in distinctly different ways. The reduction potential of the fluorophore is essentially determined by R_2, whereas the equilibrium energy ΔE_{00} is primarily influenced by changes in R_1. The presented data identify pyrazoline fluorophores as a versatile platform for the development of PET-based cation fluorescent sensors. Cell permeability, low toxicity, and high quantum yield render the fluorophore also attractive for biological applications. On the basis of the results presented in this study, we recently designed a fluorescent chemosensor for the highly specific detection of monovalent copper in aqueous solution.

Acknowledgment. Financial support from the Georgia Institute of Technology is gratefully acknowledged. Computations were supported by the Center for Computational Molecular Science and Technology at the Georgia Institute of Technology and partially funded through a Shared University Research (SUR) grant from IBM and the Georgia Institute of Technology. We also thank Sarah Shealy and David Bostwick for mass spectral data, Raxit Patel for performing the incubation experiments and flow cytometric analysis, Dr. David Sherrill for helpful discussions, Dr. Harish Radhakrishna for using his fluorescence microscope, Dr. Mira Jasowicz for her support of the electrochemical measurements, and John Cody for a critical review of the manuscript.

Supporting Information Available: Synthesis and spectroscopic characterization of derivatives **1**−**6**, details of X-ray structural acquisition and analysis (CIF files), and additional information as mentioned in the text. This material is available free of charge via the Internet at http://pubs.acs.org. The crystallographic data for the structural analysis have been deposited with the Cambridge Crystallographic Data Centre. Copies of this information may be also obtained free of charge from The Director, CCDC, 12 Union Road, Cambridge CB21EZ, UK (Fax +44-1223-336033; E-mail deposit@ccdc.cam.ac.uk or http://www.ccdc.cam.ac.uk).

JA028266O